GeoStorage

Vol. 1, No. 1, p. 56-70, 2025

Original article

# A Study of Stability and Pericavity Strain in an Underground Cavern Group for Compressed Air Energy Storage

Zhenchuan Han*, Mingming Fan, Dabao Xu, Guanghui Bi

*China Petroleum Pipeline Engineering Corporation, Langfang 065000, China*

**Keywords:**

Compressed air energy storage
cavern group
numerical simulation
intersecting region
layout parameters

**Cited as:**

Han ZC, Fan MM, Xu DB, et al. 2025. A Study of Stability and Pericavity Strain in an Underground Cavern Group for Compressed Air Energy Storage. *GeoStorage*, 1(1), 56-70.
https://doi.org/10.46690/gs.2025.01.04

**Abstract:**

The stability of underground caverns for compressed air energy storage (CAES) is critical for safe operation under high internal pressure conditions. With the development of large-scale CAES power plants, a single storage cavern can no longer meet energy storage demands, making the study of cooperative stability in cavern groups of significant engineering importance. Based on a three-dimensional numerical simulation method, this study establishes a cavern group model to systematically investigate the influence of burial depth, cavern diameter, and spacing on surrounding rock deformation and plastic zone distribution, with a particular focus on the stability of intersecting regions. The results indicate that: (1) Surrounding rock deformation decreases with increasing burial depth but exhibits an upward trend with larger cavern diameters. When the spacing exceeds 1.5D, the deformation gradually stabilizes. (2) Under an operating pressure of 15 MPa, the optimal layout parameters for the cavern group are a burial depth of 200 m, a cavern diameter of 5 m, and a spacing of 1.5D. (3) Displacement in intersecting regions is generally higher than in single-cavern sections, particularly at the connection between vertical shafts and main caverns, where deformation shows asymmetry, with greater displacement on the side adjacent to neighboring caverns, indicating significant interaction effects within the cavern group. This study provides a theoretical basis for the optimal design of underground CAES cavern groups under high internal pressure conditions.

## 1 Introduction

Under the global energy transition and the promotion of ”dual-carbon” goals, compressed air energy storage (CAES) has emerged as a research hot spot in large-scale energy storage due to its advantages of large storage capacity, long lifespan, and low cost (Crotogino et al., 2001; Budt et al., 2016; Chen et al., 2016; Li et al., 2018; Sun et al., 2025; Zhang et al., 2024). Large-scale CAES systems primarily rely on underground storage caverns, where rock masses serve as the main load-bearing structures, offering higher economic efficiency compared to above ground storage facilities. Underground storage solutions can utilize various geological formations, including salt caverns formed by salt layer dissolution (Yang et al., 2015; Sun et al., 2024), lined rock caverns, abandoned mines, and aquifers (Jia et al., 2015). However, during construction and operation, salt caverns may undergo significant contraction and deformation under long-term cyclic loading, while high-pressure air can induce salt particle-induced corrosion on mechanical surfaces. Additionally, the uneven distribution of salt deposits and complex geological conditions constrain site selection for storage facilities (Zhao et al., 2023a,b; Han et al., 2022). Aquifer-based geological structures, though economically advantageous due to their porous nature, present challenges such as structural complexity that introduces construction uncertainties and high permeability that reduces operational efficiency (Li et al., 2021; Wang et al., 2021; Tooseh et al., 2018). Abandoned mine tunnels significantly reduce construction costs but still face issues related to stability concerns, renovation difficulties, and limited site availability (Xu et al., 2021). In recent years, artificially excavated hard-rock caverns have become a critical development direction for novel CAES systems, owing to their site flexibility

Yandy Scientific Press

* Corresponding author.
*E-mail address*: hzc19972021@163.com (Han ZC); 779375775@qq.com (Fan MM); XDB20250415@163.com (Xu DB); BGH0415@163.com (Bi GH)

Received Jul. 28, 2025; revised Aug. 20, 2025; accepted Sep. 4, 2025; available online Sep. 12, 2025.

and high controllability (Xu et al., 2022; Tunsakul et al., 2013).

The stability of surrounding rock in CAES underground caverns under long-term cyclic high internal pressure loading and multi-field coupling effects(temperature-air pressure-stress) has become a critical and challenging focus in current research. In recent years, scholars worldwide have achieved significant progress in the study of CAES cavern stability. Fang et al. innovatively established a thermo-hydro-mechanical (THM) coupled analysis model to systematically investigate the influence of complex thermodynamic processes on the air-tightness of concrete-lined caverns (Fang et al., 2024). Li et al. developed a finite element model incorporating multi-field coupling effects and reinforced concrete structures, revealing the dynamic evolution of mechanical displacement and stress fields in surrounding rock through in-depth analysis (Li et al., 2023). Ma et al. proposed a novel thermo-gas-mechanical (T-GM) coupling theory that integrates gas seepage effects (Ma et al., 2022). Zhou et al. advanced an analytical solution to quantitatively characterize the mechanical response induced by coupled air pressure-temperature variations in lined rock caverns (Zhou et al., 2015a). Xia et al. further introduced a simplified unified analytical model that couples heat exchange between compressed air and surrounding rock, enabling precise prediction of temperature-pressure evolution within caverns (Xia et al., 2015). Chen et al. focused on the impact of the Excavation Damaged Zone (EDZ) on the long-term stability of CAES caverns, providing critical insights for engineering safety assessments (Chen and Wang, 2022).

Despite existing achievements providing references for CAES cavern design, the following limitations persist: Lack of systematic quantification regarding the synergistic influence mechanisms of multi-parameters (e.g., burial depth, cavern diameter, spacing) in cavern groups. Insufficient research on the stability of intersecting regions and fatigue damage under cyclic loading. Compared to single caverns, the cooperative behavior of cavern groups may induce stress superposition and interconnected plastic zones, significantly amplifying the risk of surrounding rock instability. Furthermore, intersecting regions (e.g.,junctions between vertical shafts, connecting tunnels, and main caverns) are prone to stress concentration due to geometric discontinuities, becoming critical weak points for structural integrity. Therefore, systematic investigation into layout parameter optimization and stability control strategies for intersecting regions in cavern groups is imperative to ensure the safe operation of CAES systems.

To address the aforementioned challenges, this study focuses on a CAES cavern group with parallel arrangement in hard-rock formations. A combined approach of three-dimensional numerical simulation and theoretical analysis is adopted to conduct the following investigations: Systematic analysis of the influence of varying parameters-burial depth (100 m, 200 m, 300 m), cavern diameter (5 m, 7 m, 9 m, 11 m), and cavern spacing (1D, 1.5D, 2D, 2.5D, 3D)-on surrounding rock deformation and plastic zone distribution, under fixed conditions of lining thickness (50 cm), concrete grade (C35), and operating pressure (15MPa). Based on these results, optimized layout parameters for the cavern group are proposed. At the same time, we investigate the stress concentration characteristics and fatigue damage evolution mechanism of the shaft-main cavern intersection area, and evaluate its stability control factors, so as to provide reference for the design of the subsequent compressed-gas storage power plant storage reservoir group.

## 2 Establishment of numerical model of gas storage

### 2.1 Numerical model

The study object comprises a gas storage cavern group consisting of three parallel circular tunnels. The distances from the caverns to the left, right,lower, front, and rear boundaries of the model exceed three times the cavern diameter, while the distance to the upper boundary is determined by the specified burial depth. The ground surface is defined as a free boundary. Displacement constraints are imposed as follows: X-direction constraints on the left and right boundaries, Y-direction constraints on the front and rear boundaries, and X, Y, and Z-direction constraints on the lower boundary. The gas storage pressure is simulated by applying a normal load to the inner wall of the lining. A schematic diagram of the model is illustrated in Fig. 1.

### 2.2 Yield criteria and parameter selection

In the numerical simulations, the surrounding rock is assumed to be an ideal elastoplastic material governed by the Mohr-Coulomb yield criterion. This theory is a shear stress-based strength criterion that comprehensively characterizes the strength behavior of rock, particularly reflecting its significantly lower tensile strength compared to compressive strength. The shear failure and tensile failure functions are defined as follows:

$$F_s = \sigma_1 - N_\varphi \sigma_3 + 2c\sqrt{N_\varphi} \tag{1}$$

$$F_t = \sigma_3 - \sigma_t \tag{2}$$

Where is the shear stress, is the normal stress, $\phi$ is the internal friction angle, and c is the cohesion. Where $\sigma_1$is the maximum principal stress, and $\sigma_t$is the tensile strength, $\sigma_3$ is the minimum principal stress, $N_\varphi = \frac{(1+\sin\varphi)}{(1-\sin\varphi)}$

The shear failure potential function of the surrounding rock adopts a non-associated flow rule, while the tensile failure potential function uses an associated flow rule. Their expressions are as follows:

$$g_s = \sigma_1 - \sigma_3 N_\psi \tag{3}$$

$$g_t = -\sigma_3 \tag{4}$$

$$N_\psi = \frac{(1+\sin\psi)}{(1-\sin\psi)} \tag{5}$$

$\psi$ is the expansion angle of rock. ( ° ).

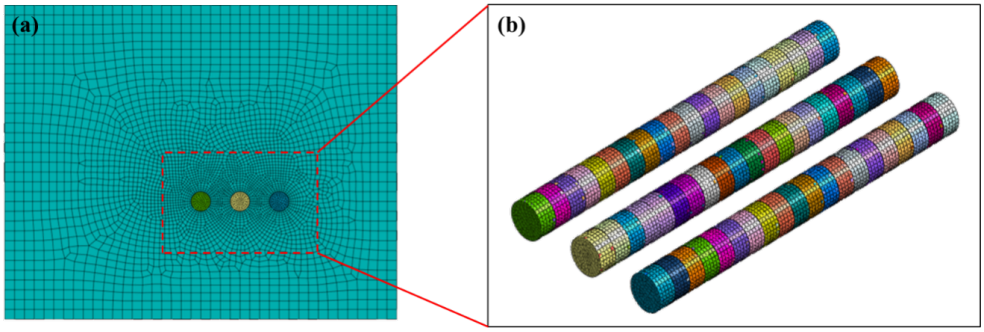


**Fig. 1** Schematic diagram of the CAES model. (a) Surrounding rock mesh; (b) Cavern mesh.

**Tab. 1** Material parameters

| Materials | Density γ/KN·m-3 | Elasticity modulus E/GPa | Internal friction angle φ/° | Cohesive force c/MPa | Poisson's ratio μ | Tensile strength /MPa |
|---|---|---|---|---|---|---|
| Surrounding rock | 26 | 28 | 50 | 15 | 0.3 | 9 |
| Lining | 25 | 31.5 | / | / | 0.17 | / |

The surrounding rock of the gas storage is granite, with the lining made of C35 concrete and assumed to be an elastic material. The initial in-situ stress only considers the self-weight stress field. Material parameters were referenced from the Code for Design of Hydraulic Tunnels, and the specific physical and mechanical parameters are listed in Tab. 1.

## 2.3 Numerical simulation scheme

During the model calculation, three main influencing factors were considered: burial depth, cavity diameter, and spacing. The burial depths were set as 100 m, 200 m, and 300 m; cavity diameters were set as 5 m, 7 m, 9 m, and 11 m; and spacings were set as 1D, 1.5D, 2D, 2.5D, and 3D (where D denotes the cavity diameter). The research schemes for the gas storage under each working condition are listed in Tab. 2.

**Tab. 2** Gas storage research program

| Research object | Circular tunnel gas storage |
|---|---|
| Depth/m | 100, 200, 300 |
| Hole diameter/m | 5, 7, 9, 11 |
| Distance between holes/m | 1D, 1.5D, 2D, 2.5D, 3D |

## 2.4 Calculation Process

The calculation is divided into four steps: Step 1: Establish initial in-situ stress equilibrium and reset displacement to zero. Step 2: Excavate caverns sequentially (each tunnel excavated in 2 m increments), deactivate the excavation and lining mesh groups, and passivate the excavated grid elements. Step 3: Install linings and activate the lining mesh groups; repeat Steps 2-3 cyclically until full excavation is completed. Step 4: Apply gas storage pressure (15 MPa) to the cavern surfaces.

# 3 Experimental results and analysis

The monitoring point configuration for the cavern group is illustrated in Fig. 2.

Vertical displacement analysis focuses on the vault (crown) and invert (floor) points of the mid-cross-section of each cavern: Left cavern: Points I1 (vault) and I3 (invert). Middle cavern: Points J1 (vault) and J3 (invert). Right cavern: Points K1 (vault) and K3 (invert).

Horizontal displacement analysis targets the haunch (sidewall) points of the mid-cross-section: Left cavern: Points I2 (left haunch) and I4 (right haunch). Middle cavern: Points J2 (left haunch) and J4 (right haunch). Right cavern: Points K2 (left haunch) and K4 (right haunch).

Coordinate system: +Y: Upward (vertical direction). +X: Rightward (horizontal direction). +Z: Inward (perpendicular to the plane of the diagram).

## 3.1 Influence of different burial depths on the stability of gas storage

### 3.1.1 Analysis of numerical simulation results

From the displacement nephograms illustrated in Fig.s 3 and 4, the following observations can be made: At a cavern burial depth of 100 m, the maximum displacement of surrounding rock reaches approximately 3.68 mm, occurring at the cavern crown with inward-directed deformation. All displacement values remain within acceptable engineering limits. The maximum Z-direction displacement of 2.36 mm is predominantly observed at the cavern floor. When the burial depth increases to 200 m, the peak surrounding rock displacement decreases to approximately 2.23 mm, maintaining its occurrence at the cavern crown but exhibiting an upward-leftward deformation vector towards the cavern interior. Concurrently, the maximum Z-direction displacement reduces to 1.53 mm, still concentrated at the cavern base. At 300 m burial depth, the maximum displacement further diminishes to 0.87 mm, retaining both the crown

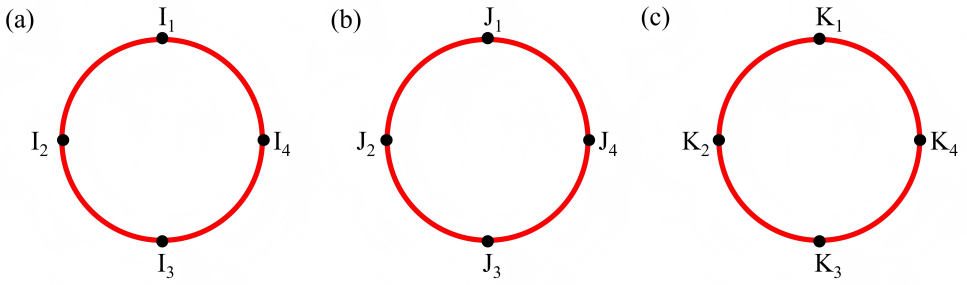


**Fig. 2** Schematic diagram of monitoring points

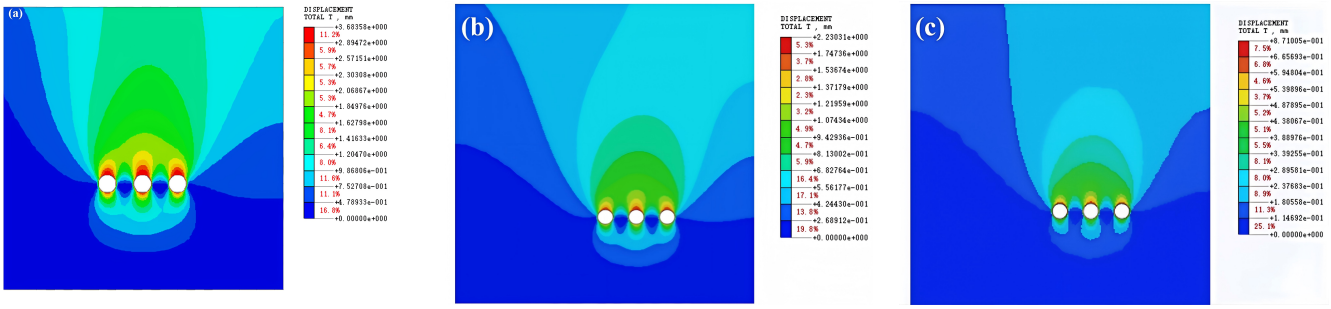


**Fig. 3** Total displacement cloud map of different buried depths (a) 100m (b) 200m (c) 300m

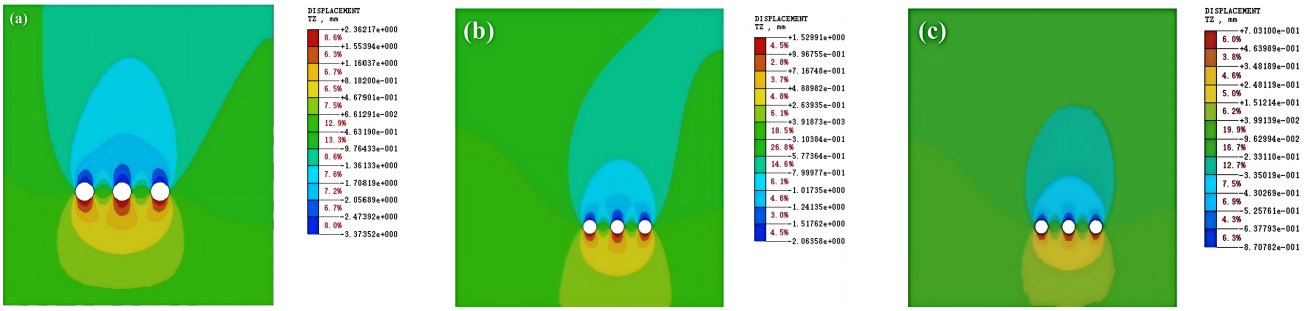


**Fig. 4** Displacement cloud map in Z direction of different buried depths (a) 100m (b) 200m (c) 300m

location and upward-leftward deformation tendency. The corresponding maximum Z-direction displacement measures 0.7 mm, continuing to manifest primarily at the cavern floor.

From the stress nephogram presented in Fig.5, the following mechanical characteristics can be interpreted: The extensive stress distribution pattern reveals relatively uniform stress redistribution across most regions, conforming to the typical stress redistribution mechanism post-tunnel excavation. Maximum tensile stress concentrations in surrounding rock predominantly occur near the crown, sidewalls, and excavation boundaries, though these values remain significantly below the tensile strength threshold of the rock mass. Conversely, elevated compressive stresses are concentrated in the floor strata and deeper rock zones, yet all measured stresses maintain sufficient safety margins below critical levels required to trigger stress-induced failure mechanisms.

From the strain nephogram depicted in Fig.6, the following deformation characteristics are revealed: At a burial depth of 100 m, the cavern exhibits an extensive deformation zone, with tensile strain concentrations predominantly observed near the crown, sidewalls, and excavation boundaries, which may induce crack initiation. Elevated compressive strains are likely concentrated in the floor strata and deeper rock masses, accompanied by interconnected deformation patterns among the left, central, and right cavern sections. When the burial depth increases to 200 m and 300 m, the deformed area progressively contracts,showing more homogeneous strain distribution across the rock mass-indicating enhanced deformation compatibility. Notably, both tensile and compressive strains maintain magnitudes well below critical thresholds for structural instability throughout all burial conditions.

The longitudinal deformation characteristics of the tunnel crown are manifested as upward displacement in the central section during through-excavation. The vertical unloading effects induced by breakthrough excavation generate localized heave in the tunnel base and surrounding soils, creating upward soil reaction forces that collectively elevate the central tunnel segment. Subsequent longitudinal constraints at both portals may result in forced upward displacement of the entire tunnel structure. Correspondingly, surface displacement monitoring reveals a characteristic deformation pattern: central section heave with portal settlement, primarily governed by three

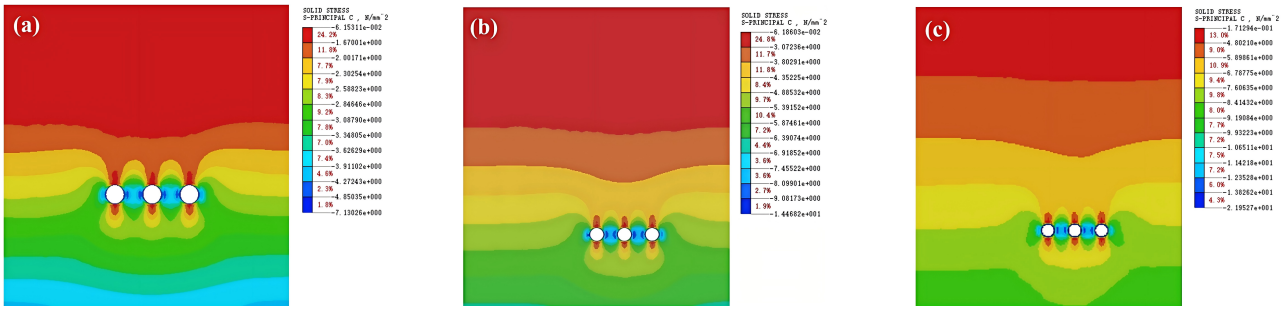


**Fig. 5** Stress cloud map of different burial depths (a) 100m (b) 200m (c) 300m

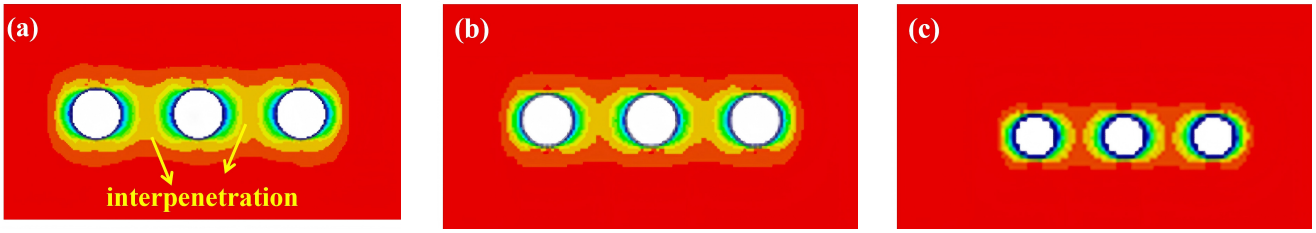


**Fig. 6** Strain cloud map at different burial depths (a) 100m (b) 200m (c) 300m

coupled mechanisms-ground loss from shallow-buried mega-section excavation, frost heave effects, and post-excavation buoyancy response. Notably, crown subsidence demonstrates positive correlation with surface settlement magnitude. Both crown displacement and base heave exhibit progressive contraction with increasing burial depth, emphasizing the necessity for real-time comparative analysis between internal and external monitoring data to implement timely deformation control strategies.

As demonstrated in Tab.3 and Fig.7 for gas storage caverns with 5 m diameter and 1D spacing, displacement magnitudes at critical monitoring points exhibitconsistent reduction with increasing burial depth. This trend quantitatively verifies the stabilizing effect of overburden pressure on excavation-induced deformations.

### 3.1.2 Analysis of perimeter rock deformation

As shown in Fig. 7(a), when the burial depth of the gas storage is 100 m, point I1 in the left cavern descended by 2.82 mm, and point I3 ascended by 1.91 mm; point J1 in the middle cavern descended by 2.91 mm, and point J3 ascended by 2.00 mm; point K1 in the right cavern ascended by 2.77 mm, and point K3 descended by 1.86 mm. The vertical displacements of points I1 and I3 in the left cavern and points K1 and K3 in the right cavern were all smaller than those in the middle cavern. When the burial depth increased to 200 m, point I1 in the left cavern ascended by 1.78 mm, and point I3 descended by 1.27 mm; point J1 in the middle cavern descended by 1.89 mm, and point J3 ascended by 1.34 mm; point K1 in the right cavern ascended by 1.79 mm, and point K3 descended by 1.26 mm. The vertical displacements of points I1 and I3 in the left cavern were basically the same as those in the right cavern. At a burial depth of 300 m, point I1 in the left cavern ascended by 0.82 mm, point I3 descended by 0.66 mm, point J1 in the middle cavern descended by 0.86 mm, and point J3 ascended by 0.70 mm; point K1 in the right cavern ascended by 0.84 mm, and point K3 descended by 0.65 mm. As the burial depth increased from 100 m to 300 m, the vertical displacements of points I1 and I3 in the left cavern, J1 and J3 in the middle cavern, and K1 and K3 in the right cavern decreased by 70.9%, 65.5%, 70.5%, 65%, 69.7%, and 65.1%, respectively.

**Tab. 3** Displacements at key points of gas storage at different burial depths (Simplified)

| | Key monitoring points | Depth/m | | |
|---|---|---|---|---|
| | | 100 | 200 | 300 |
| Vertical displacement/mm | I1 | -2.82 | -1.78 | -0.82 |
| | I3 | 1.91 | 1.27 | 0.66 |
| | J1 | -2.91 | -1.89 | -0.86 |
| | J3 | 2.00 | 1.34 | 0.70 |
| | K1 | -2.77 | -1.79 | -0.84 |
| | K3 | 1.86 | 1.26 | 0.65 |
| Horizontal displacement/mm | I2 | -2.69 | -1.56 | -0.55 |
| | I4 | 3.13 | 1.78 | 0.65 |
| | J2 | -2.99 | -1.79 | -0.63 |
| | J4 | 3.00 | 1.76 | 0.64 |
| | K2 | -2.97 | -1.77 | -0.62 |
| | K4 | 2.72 | 1.59 | 0.56 |

As shown in Fig. 7(b), when the burial depth of the gas storage is 100 m, the I2 point of the left cavern moves 3.13 mm to the left, and the I4 point moves 3.13 mm to the right; the J2 point of the middle cavern moves 2.99 mm to the left, and the J4 point moves 3.00 mm to the right; the K2 point of the right cavern moves 2.97 mm to the left, and the K4 point moves 2.72 mm to the right. At a burial depth of 200 m, the I2 point of the left cavern moves 1.56 mm to the left, and the I4 point moves

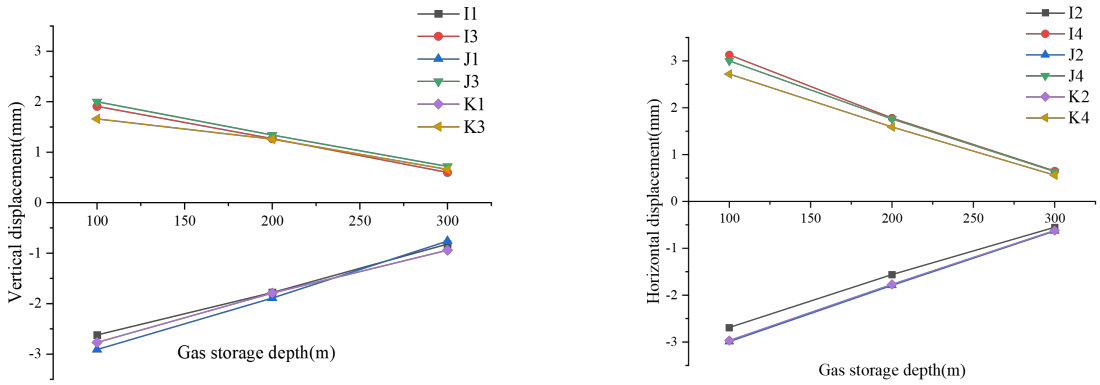


a Vertical displacement b Horizontal displacement

**Fig. 7** Deformation curve of surrounding rock with different burial depth

1.78 mm to the right; the J2 point of the middle cavern moves 1.79 mm to the left, and the J4 point moves 1.76 mm to the right; the K2 point of the right cavern moves 1.77 mm to the left, and the K4 point moves 1.59 mm to the right. When the burial depth increases to 300 m, the I2 point of the left cavern moves 0.55 mm to the left, the I4 point moves 0.18 mm to the right, the J2 point of the middle cavern moves 0.28 mm to the left, and the J4 point moves 0.65 mm to the right. The horizontal displacement of the I4 point in the left cavern is the largest, while that of the I2 point in the left cavern is the smallest; the displacements of the J2 and J4 points in the middle cavern are nearly equal. As the burial depth increases from 100 m to 300 m, the horizontal displacements of the I2 and I4 points in the left cavern, J2 and J4 points in the middle cavern, and K2 and K4 points in the right cavern decrease by 79.6%, 79.2%, 78.9%, 78.7%, 79.1%, and 79.4%, respectively. The variation in horizontal displacement is significantly larger than that in vertical displacement.

Analysis reveals that as the burial depth of the gas storage increases, the self-weight of the surrounding rock increases progressively. At a burial depth of 100 m, the self-weight of the surrounding rock is much smaller than the gas storage pressure, causing significant outward deformation of the gas storage under the action of the gas pressure. As the burial depth increases, the self-weight of the surrounding rock approaches the gas storage pressure, leading to a reduction in the deformation of the gas storage.

### 3.1.3 Analysis of the plastic zone of the surrounding rock

The front view of the plastic zone distribution in the surrounding rock of gas storage caverns with different burial depths is shown in Fig. 8, where the cavity diameter is 5 m and the spacing is 10 m. As the burial depth increases, the surrounding rock gradually transitions from large plastic deformation to elastic deformation. When the burial depth is 100 m, plastic zones form at the bottom and side surfaces of all three caverns, and connected plastic zones develop between the tunnels, with particularly severe plastic zones occurring in the arch waist regions of the left and right caverns. When the burial depth increases to 200 m and 300 m, the plastic deformation of the tunnels is significantly reduced. This indicates that below a burial depth of 200 m, the tunnels will not undergo plastic deformation under a gas storage pressure of 15 MPa. Combining with the variation law of the gas storage deformation with burial depth, it can be concluded that burial depth has a significant impact on the gas storage structure. Compared with the gas storage with a burial depth of 100 m, those with burial depths of 200 m and 300 m are relatively more stable.

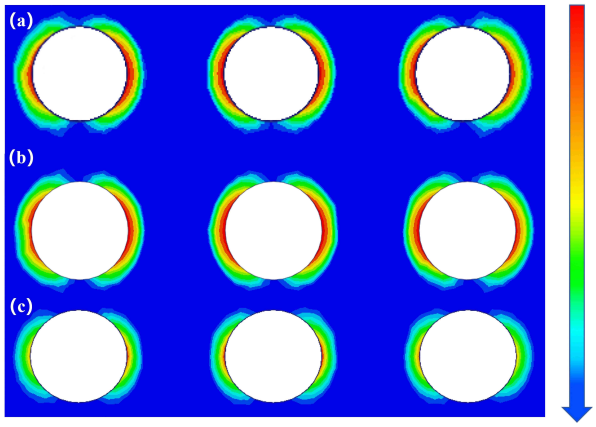


**Fig. 8** Distribution of plastic zones in the surrounding rock at different burial depths (a) 100m (b) 200m (c) 300m

Overall, the burial depth has a significant impact on the deformation of the surrounding rock and the distribution of the plastic zone in gas storage. The greater the burial depth, the smaller the vertical, horizontal, and axial displacements of the surrounding rock, which gradually transitions from plastic deformation to elastic deformation. When the burial depth of the gas storage is 200 m and 300 m, the surrounding rock is relatively stable.

## 3.2 Influence of different hole diameters on gas storage stability

### 3.2.1 Analysis of numerical simulation results

As shown in the surrounding rock displacement nephograms of Fig.s 9 and 10, when the cavern diameter is 5 m, the maximum displacement of the surrounding rock is approximately 2.12 mm, occurring at the arch crown of the cavern with a direction toward the upper left inside the cavern. The maximum Z-direction displacement is approximately 1.43 mm, primarily occurring at the cavern floor. When the cavern diameter is

7 m, the maximum surrounding rock displacement is around 3.63 mm, also at the arch crown, with a direction toward the upper interior of the cavern. The maximum Z-direction displacement is approximately 2.10 mm at the cavern floor, and the deformations of each cavern are interconnected. For cavern diameters of 9 m and 11 m, the maximum surrounding rock displacements are 5.22 mm and 7.81 mm, respectively, both at the arch crown. The maximum Z-direction displacements are approximately 2.84 mm and 3.95 mm, respectively, primarily at the cavern floor, with no interconnection between the caverns.

As shown in the surrounding rock stress nephogram of Fig. 11, the stress distribution is relatively widespread, indicating that stress release is uniform in most areas, which is consistent with the typical law of stress redistribution after tunnel excavation. The maximum principal stress in the surrounding rock tends to exhibit tensile stress concentration near the arch crown, sidewalls, or excavation surface, but this is far less than the tensile strength of the surrounding rock. The floor and deep portions of the surrounding rock may bear higher compressive stress. The relatively uniform stress distribution suggests a stable stress field; however, for deeply buried tunnels or complex geological conditions, changes in stress direction may pose a potential risk of structural plane sliding. Compared with the cavern with a diameter of 5 m, stress concentration is more pronounced in caverns with other diameters, which may lead to crushing or shear failure.

**Tab. 4** Displacements at key monitoring points of gas storage reservoirs with different hole diameters

| Displacement type | Key monitoring point | Hole diameter (m) | | | |
|---|---|---|---|---|---|
| | | 5 | 7 | 9 | 11 |
| Vertical displacement (mm) | I1 | -1.78 | -2.73 | -3.63 | -5.77 |
| | I3 | 1.27 | 1.66 | 2.19 | 2.69 |
| | J1 | -1.89 | -2.90 | -4.19 | -6.15 |
| | J3 | 1.34 | 1.75 | 2.13 | 2.92 |
| | K1 | -1.79 | -2.73 | -3.83 | -5.74 |
| | K3 | 1.26 | 1.68 | 2.26 | 2.94 |
| Horizontal displacement (mm) | I2 | -1.56 | -2.87 | -4.27 | -6.27 |
| | I4 | 1.78 | 3.14 | 4.29 | 6.27 |
| | J2 | -1.79 | -3.14 | -4.29 | -7.23 |
| | J4 | 1.76 | 3.07 | 4.41 | 7.21 |
| | K2 | -1.78 | -3.07 | -4.18 | -7.05 |
| | K4 | 1.59 | 2.52 | 4.22 | 5.86 |

As observed from the surrounding rock strain nephogram in Fig.12, as the cavern diameter increases, the area of the deformed region in the surrounding rock gradually expands. Tensile strain concentration occurs near the arch crown, sidewalls, or excavation surface, which may lead to cracking. The uniform strain distribution indicates good deformation compatibility. The floor or deep portions of the surrounding rock may experience high compressive strain. Except for the cavern with a diameter of 5 m, the deformations of the left, middle, and right caverns are interconnected, potentially causing a series of strain concentrations that affect cavern stability.

### 3.2.2 Analysis of perimeter rock deformation

As shown in Tab. 4 and Fig. 13, when the burial depth is 200 m and the spacing is 15 m, the displacement values at each point in the surrounding rock of gas storage caverns increase continuously as the cave diameter of the gas storage caverns increases. As shown in Fig. 13(a), when the cave diameters are 5 m, 7 m, 9 m, and 11 m, the vertical displacement at point I1 of the left cavern decreases by 1.78 mm, 2.73 mm, 3.63 mm, and 5.77 mm, respectively; the vertical displacement at point I3 of the left cavern rises by 1.27 mm, 1.66 mm, 2.19 mm, and 2.69 mm, respectively; the vertical displacement at point J1 of the middle cavern decreases by 1.89 mm, 2.90 mm, 4.19 mm, and 6.15 mm, respectively; and the vertical displacement at point J3 of the middle cavern rises by 1.34 mm, 1.75 mm, 2.13 mm, and 2.92 mm, respectively. As the cave diameter increases from 5 m to 11 m, the vertical displacement at the arch crown continuously increases, while the vertical displacement at the arch bottom rises slightly.

Fig. 13(b) shows that the horizontal displacement at the arch waist of the gas storage caverns increases linearly with the increase in cave diameter, with the horizontal displacement at point J2 of the middle cavern being the largest and that at point I2 of the left cavern being the smallest. When the cave diameter is 5 m, the horizontal displacements at points I2 and I4 of the left cavern, points J2 and J4 of the middle cavern, and points K2 and K4 of the right cavern are 1.56 mm, 1.78 mm, 1.79 mm, 1.76 mm, 1.78 mm, and 1.59 mm, respectively. When the cave diameter is 11 m, these values become 6.27 mm, 6.27 mm, 7.23 mm, 7.21 mm, 7.05mm, and 5.86 mm, respectively, representing increases of 75.1%, 71.6%, 75.2%, 75.6%, 74.8%, and 72.9%. The increase in horizontal displacement is significantly larger than that in vertical displacement.

### 3.2.3 Analysis of the plastic zone of the surrounding rock

The front view of plastic deformation in the surrounding rock of gas storage caverns with different cave diameters at a burial depth of 200 m and a spacing of 15 m is shown in Fig. 62. The Fig. indicates that the area of the plastic deformation region in each cavern is smaller compared to that of caverns at a burial depth of 100 m. Analysis shows that when the burial depth of the gas storage caverns is 200 m and the spacing is 15 m, the self-weight of the surrounding rock is sufficient to balance the gas storage pressure, ensuring that the stress applied to the surrounding rock is less than its failure strength.Thus, the surrounding rock does not undergo failure and remains stable at all times. When the cave diameter of the gas storage cavern increases, the excavation length decreases, the working space increases, the construction period is correspondingly shortened, and the required construction costs are reduced. To save costs, a cave diameter of 5 m for each gas storage cavern is considered reasonable.

## 3.3 Effect of different spacing on the stability of gas storage reservoirs

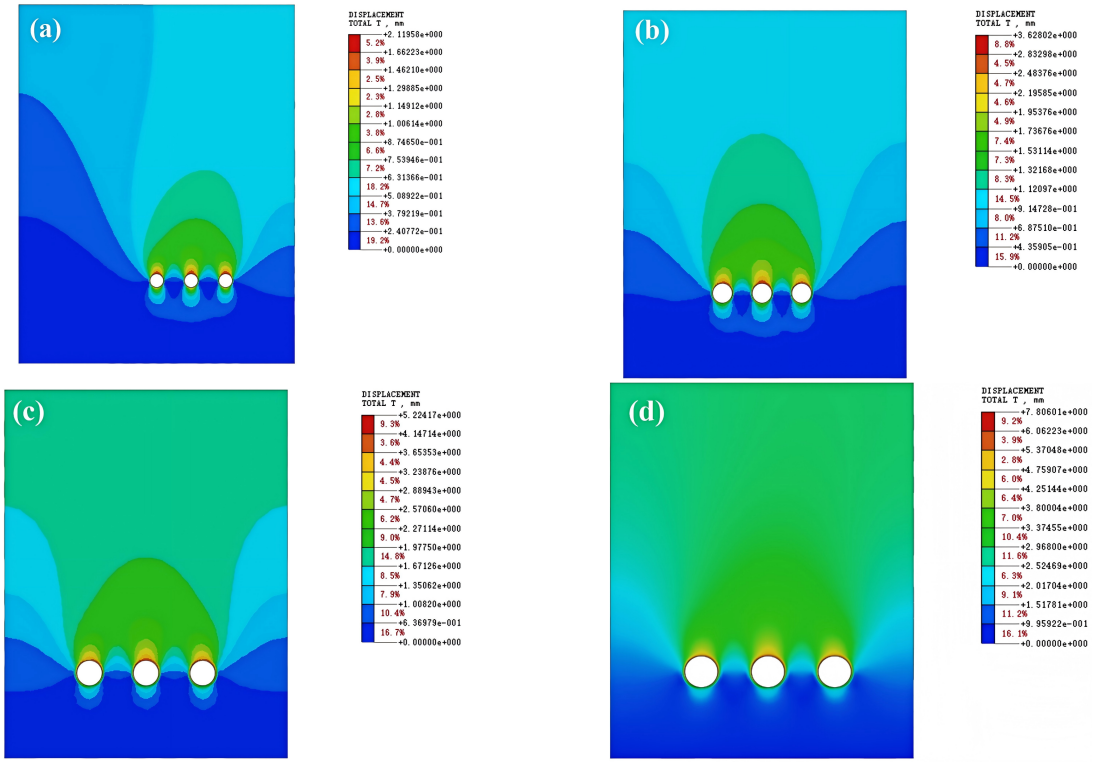


**Fig. 9** Cloud diagram of total displacement distribution of surrounding rock with different diameters at 200m depth (a) 5m (b) 7m (c) 9m (d) 11m

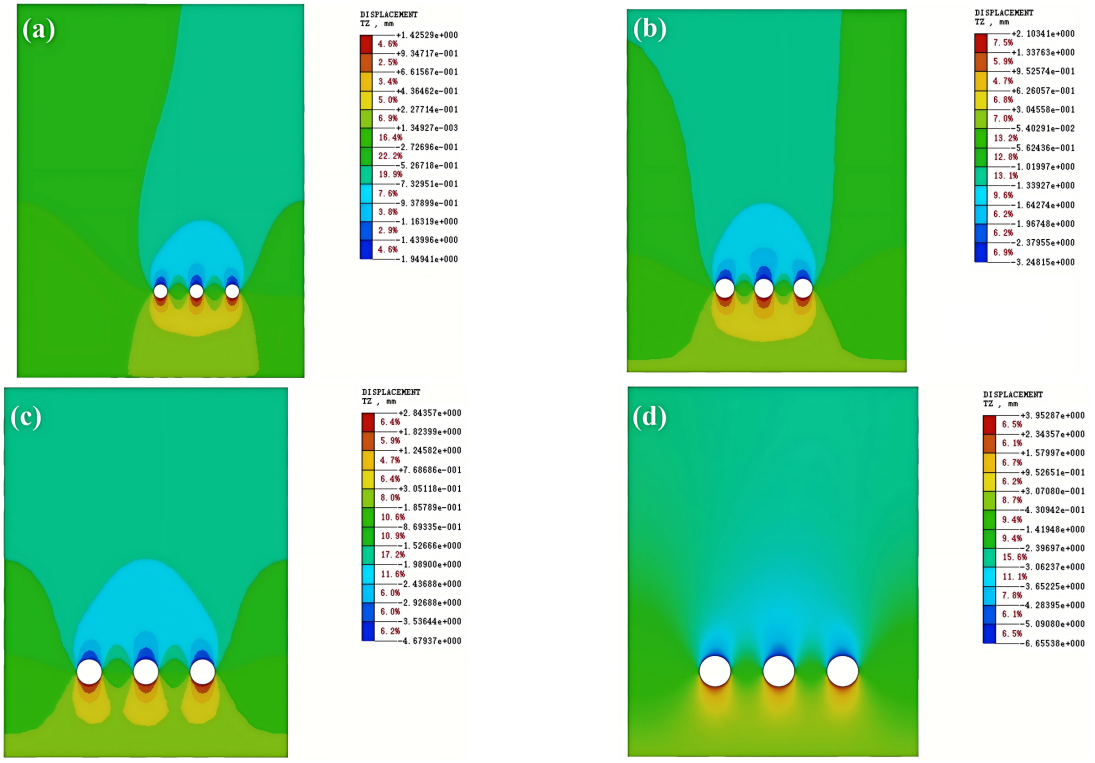


**Fig. 10** Z-direction displacement distribution of surrounding rock with different hole diameters at 200m depth (a) 5m (b) 7m (c) 9m (d) 11m

### 3.3.1 Analysis of numerical simulation results

As shown in the surrounding rock displacement nephograms of Fig.s 15 and 16, the total maximum displacement value of the surrounding rock is approximately 2.23mm, with the maximum displacement occurring at the arch crown of the cavern when the

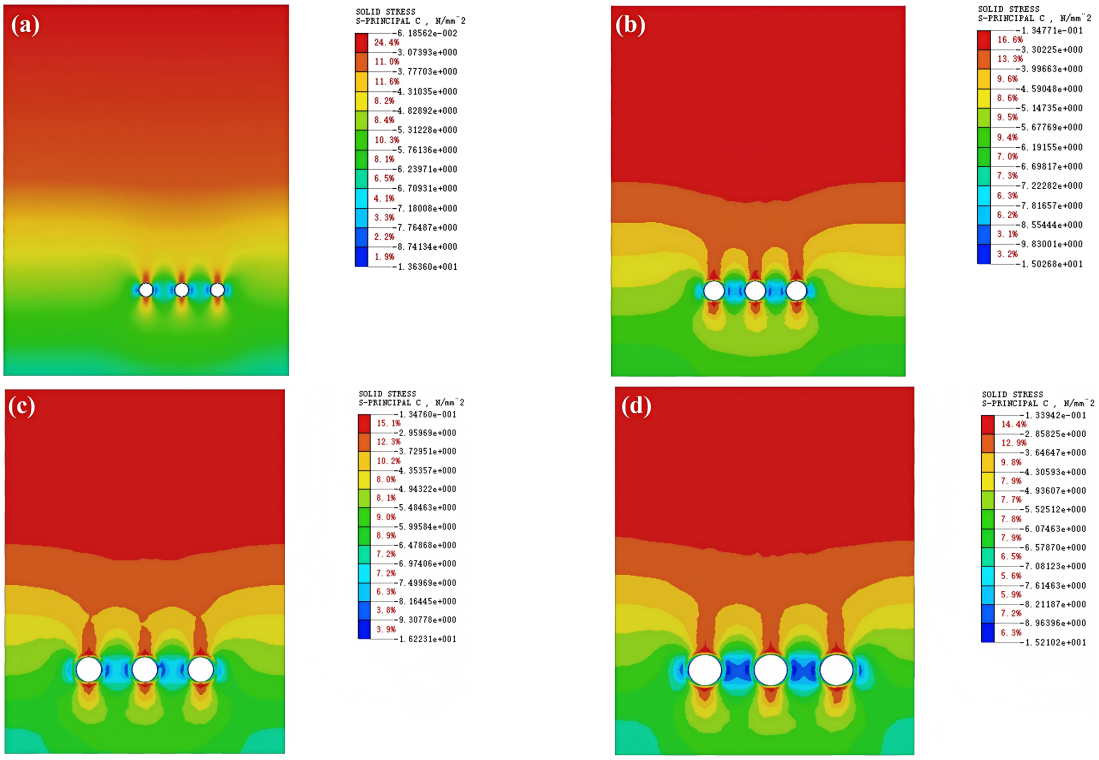


**Fig. 11** Minimum principal stress of surrounding rock with different diameters at 200m depth (a) 5m (b) 7m (c) 9m (d) 11m

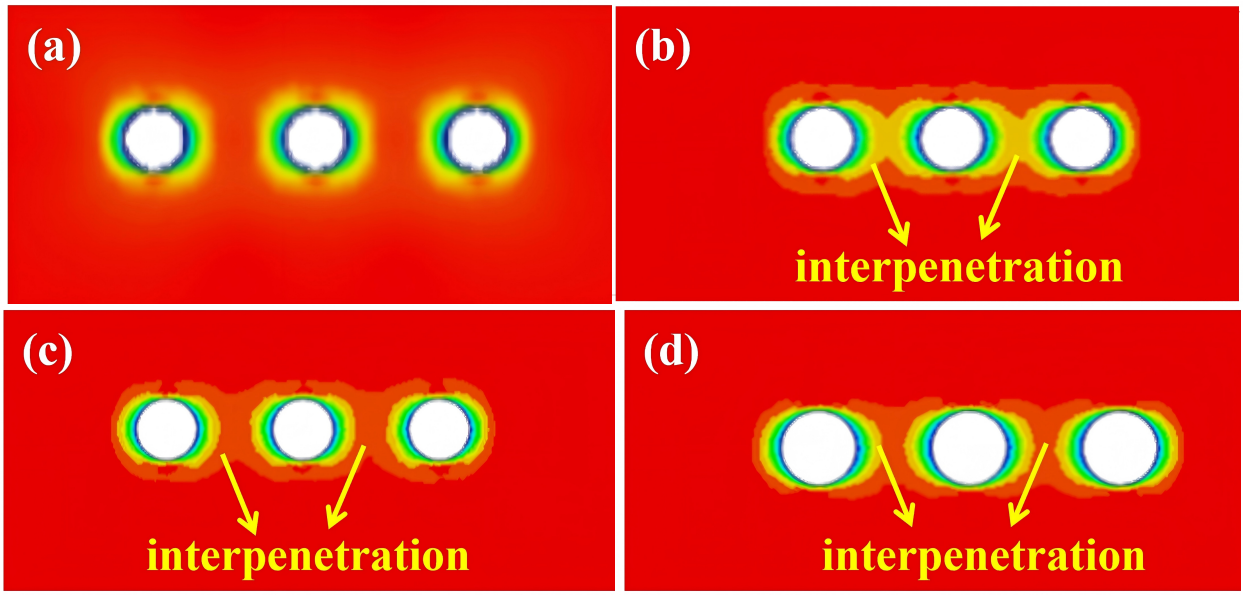


**Fig. 12** Minimum principal strain of surrounding rock with different diameters at 200m depth (a) 5m (b) 7m (c) 9m (d) 11m

cavern spacing is 5 m, and the displacement direction is toward the interior of the cavern. As the cavern spacing increases, the displacement values at the arch crown and floor of the cavern gradually decrease. The Z-direction displacement primarily occurs at the cavern floor. With the increase in spacing, the vertical and horizontal displacements of the surrounding rock first decrease and then remain constant. The horizontal displacements at the left arch waist of the left cavern and the right arch waist of the right cavern continuously decrease and tend to stabilize, while the horizontal displacements at the arch crowns of other positions gradually decrease and stabilize as well.

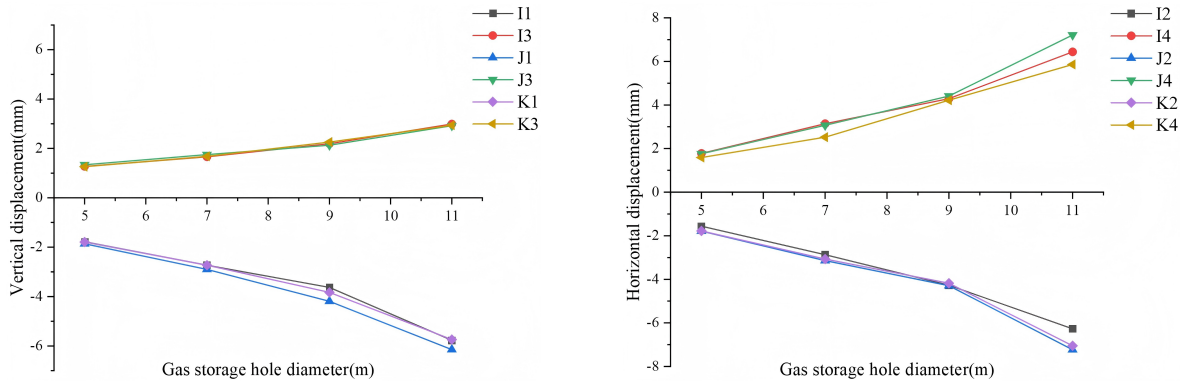


a Vertical displacement b Horizontal displacement

**Fig. 13** Deformation curves of surrounding rocks with different hole diameters

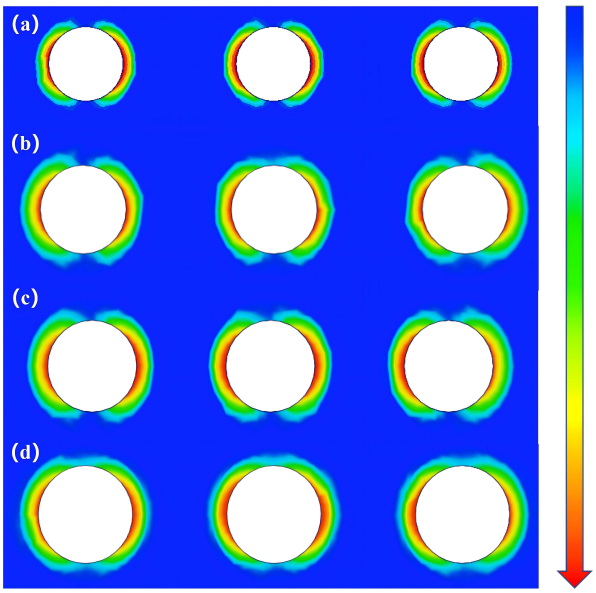


**Fig. 14** Plastic deformation of surrounding rock with different hole diameters (a) 5m (b) 7m (c) 9m (d) 11m

As shown in the surrounding rock stress nephogram of Fig. 17, the stress distribution is relatively widespread, indicating that stress release is uniform in most areas, which is consistent with the typical law of stress redistribution after tunnel excavation. The maximum principal stress in the surrounding rock tends to exhibit tensile stress concentration near the arch crown, sidewalls, or excavation surface, but this is far less than the tensile strength of the surrounding rock. The relatively uniform stress distribution suggests a stable stress field. As the cavern spacing increases, the phenomenon of surrounding rock stress concentration decreases.

As observed from the surrounding rock strain nephogram in Fig. 18, when the cavern spacing is 10 m, the area of the deformed region in the surrounding rock is relatively large. Tensile strain concentration occurs near the arch crown, sidewalls, or excavation surface, which may lead to cracking. The floor or deep portions of the surrounding rock may experience high compressive strain, and the deformations of the left, middle, and right caverns are interconnected. As the cavern spacing increases, the phenomenon of strain concentration significantly weakens, and the strain distribution becomes uniform, indicating good deformation compatibility.

### 3.3.2 Analysis of perimeter rock deformation

Tab. 5 and Fig. 19 present the deformation values and curves of key points in the surrounding rock of each gas storage cavern under different spacing conditions when the burial depth is 200 m and the cave diameter is 5 m. As shown in Fig. 19(a), when the spacing between gas storage caverns increases from 1D to 3D, the vertical displacement of point I1 in the left cavern decreases from 1.78 mm to 1.63 mm, the vertical displacement of point I3 in the left cavern decreases from 1.27 mm to 1.21 mm, the vertical displacement of point J1 in the middle cavern decreases from 1.86 mm to 1.70 mm, and the vertical displacement of point J3 in the middle cavern decreases from 1.34 mm to 1.17 mm. The vertical displacements of the surrounding rock in each cavern change slightly.

**Tab. 5** Displacement of key monitoring points in gas storage reservoirs with different hole spacings

| Displacement type | Key monitoring point | Hole spacing (m) | | | | |
|---|---|---|---|---|---|---|
| | | 10 | 15 | 20 | 25 | 30 |
| Vertical displacement (mm) | I1 | -1.78 | -1.70 | -1.67 | -1.64 | -1.63 |
| | I3 | 1.27 | 1.22 | 1.22 | 1.21 | 1.21 |
| | J1 | -1.86 | -1.76 | -1.72 | -1.70 | -1.70 |
| | J3 | 1.34 | 1.25 | 1.21 | 1.19 | 1.17 |
| | K1 | -1.79 | -1.72 | -1.71 | -1.70 | -1.71 |
| | K3 | 1.26 | 1.21 | 1.18 | 1.16 | 1.15 |
| Horizontal displacement (mm) | I2 | -1.56 | -1.54 | -1.53 | -1.53 | -1.52 |
| | I4 | 1.78 | 1.69 | 1.66 | 1.57 | 1.58 |
| | J2 | -1.79 | -1.67 | -1.62 | -1.66 | -1.59 |
| | J4 | 1.76 | 1.74 | 1.67 | 1.68 | 1.56 |
| | K2 | -1.78 | -1.69 | -1.64 | -1.62 | -1.62 |
| | K4 | 1.59 | 1.59 | 1.57 | 1.57 | 1.62 |

From Fig. 19(b), when the spacing is 1D, 1.5D, 2D, 2.5D,

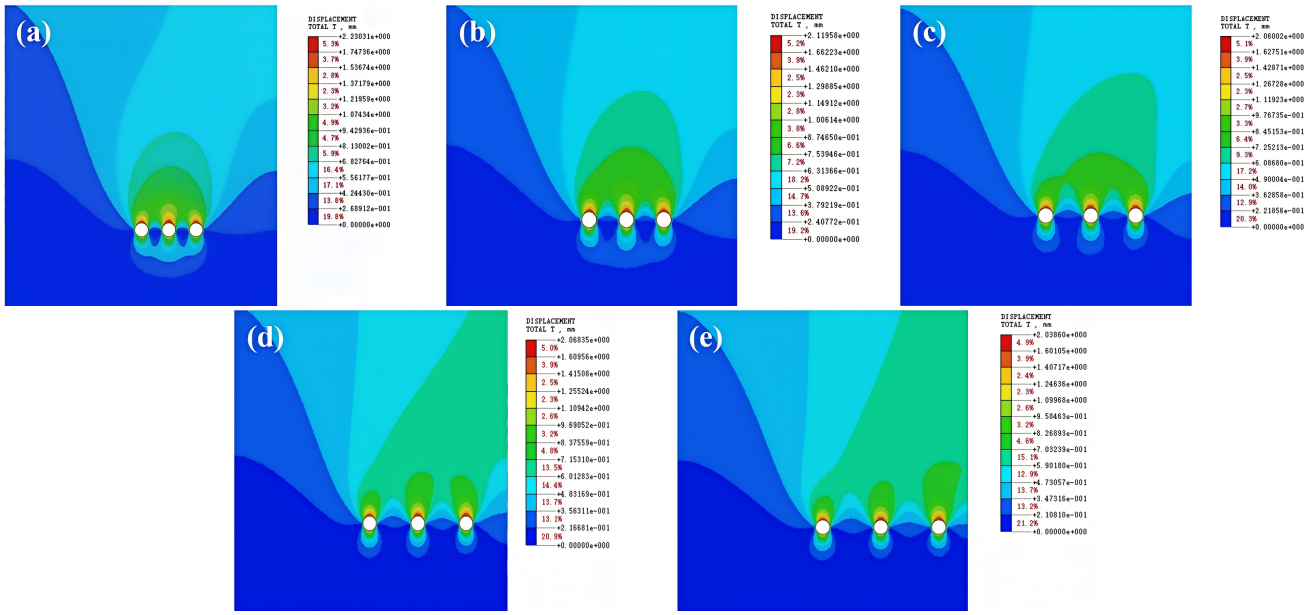


**Fig. 15** Total displacement cloud for different spacing (a) 10m (b) 15m (c) 20m (d) 25m (e) 30m

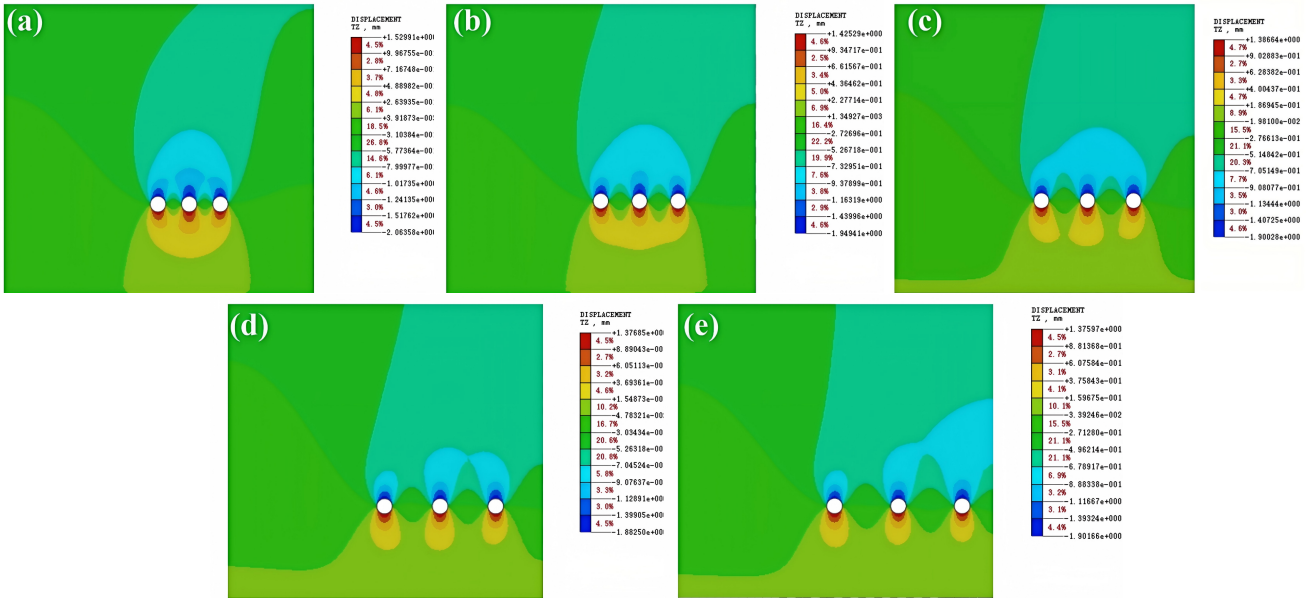


**Fig. 16** Displacement clouds in Z-direction for different spacings (a) 10m (b) 15m (c) 20m (d) 25m (e) 30m

and 3D, the horizontal displacements of point I2 in the left cavern are 1.56 mm, 1.54 mm, 1.53 mm, 1.53mm, and 1.52 mm, respectively; the horizontal displacements of point I4 in the left cavern are 1.78 mm, 1.69 mm, 1.66 mm, 1.57 mm, and 1.58 mm, respectively;the horizontal displacements of point J4 in the middle cavern are 1.76 mm, 1.74 mm, 1.67 mm, 1.68 mm, and 1.56 mm, respectively; and the horizontal displacements of point J2 in the middle cavern are 1.79 mm, 1.67 mm, 1.62 mm, 1.66 mm, and 1.59 mm, respectively. The displacements of points K2 and K4 in the right cavern are basically consistent with those in the left and middle caverns. The horizontal displacements of each point in the caverns decrease with the increase in spacing,with a gradually decreasing rate of decrease, while the vertical displacements of each point decrease slightly and tend to stabilize as the spacing increases.

Analysis shows that the gas storage pressure inside point I4 of the left cavern acts in the opposite direction to the displacement direction of the left archwaist of the middle cavern, exerting a constraining effect on its deformation. When the spacing increases, the constraining effect on the left arch waist of the middle cavern decreases, leading to an increase in horizontal displacement. The same mechanism applies to the horizontal displacement changes at the right arch waist of the middle cavern and the left arch waist of the left cavern. The gas storage pressure inside the middle cavern acts in the same direction as the displacement direction of the left arch waist of the left cavern, promoting its deformation. When the spacing increases, this promoting effect weakens, causing the horizontal displace-

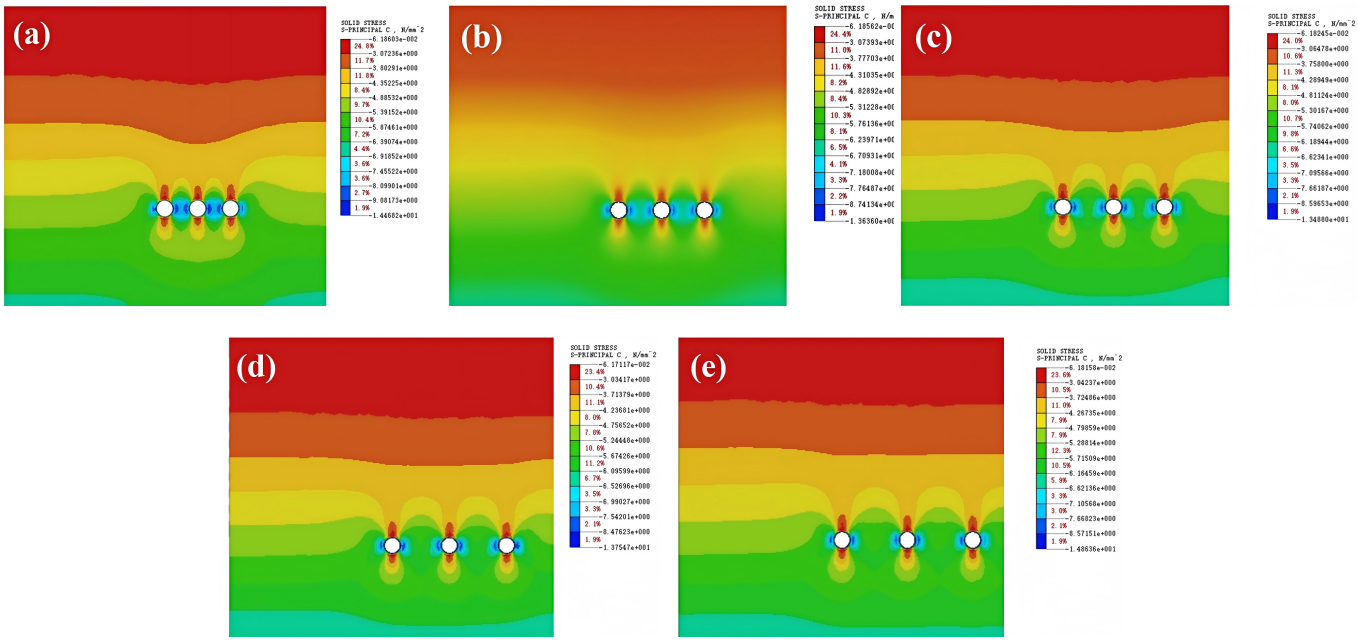


**Fig. 17** Stress of surrounding rock at 200m depth with different hole spacing (a) 10m (b) 15m (c) 20m (d) 25m (e) 30m

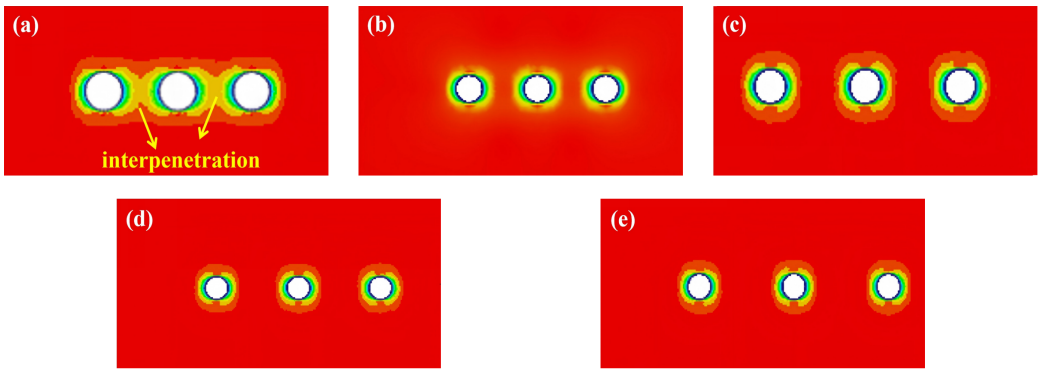


**Fig. 18** Main strain of surrounding rock with different hole spacing at 200m depth (a) 10m (b) 15m (c) 20m (d) 25m (e) 30m

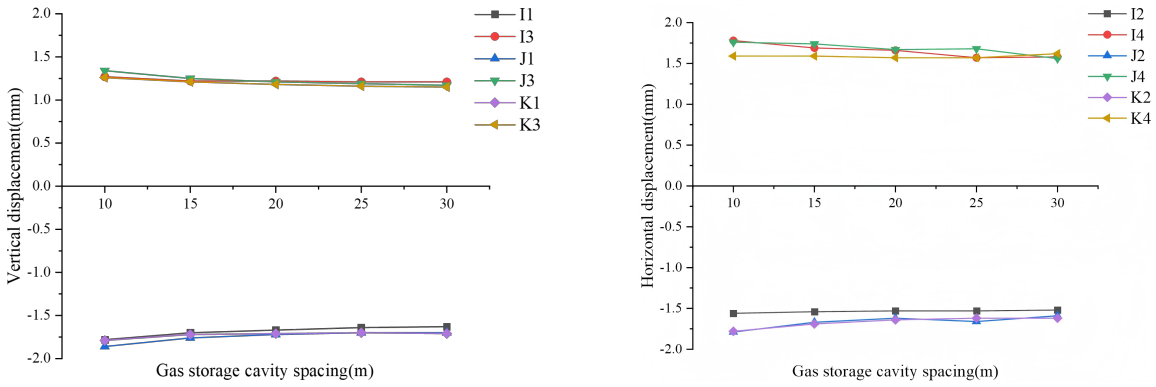


a Vertical displacement b Horizontal displacement

**Fig. 19** Deformation curves of surrounding rock with different spacing

ment at the left arch waist of the left cavern to decrease.

### 3.3.3 Analysis of the plastic zone of the surrounding rock

Fig. 20 presents front views of plastic zone distribution in surrounding rock under different spacing conditions for underground gas storage at 200 m burial depth with 5m cavern diameter. The results indicate that no plastic failure was observed in gas storage caverns with spacings of 1D, 1.5D, 2D, 2.5D,

and 3D. Combined with deformation analysis of surrounding rock under varying spacings, the gas storage maintains stability within the spacing range of (1-3)D. Notably, larger spacing configurations require greater ground surface occupation and consequently higher construction costs. To optimize economic efficiency while ensuring operational safety, a cavern spacing of 1.5D proves to be the most reasonable design parameter. This configuration achieves effective balance between spatial utilization and cost-effectiveness while maintaining structural integrity under operational conditions.

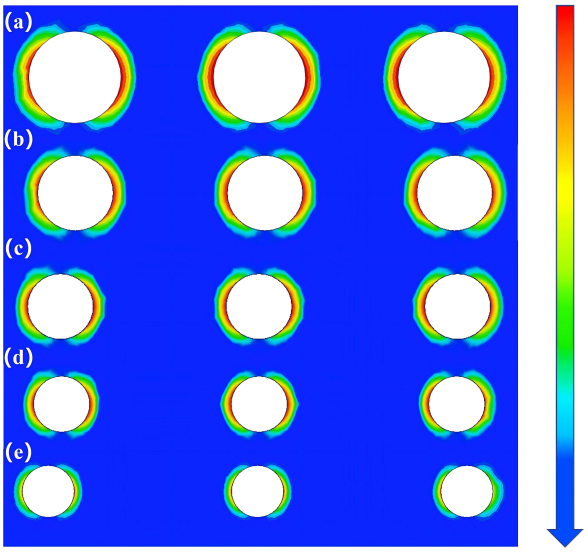


**Fig. 20** Distribution of plastic zones in the surrounding rock at different spacing (a) 10m (b) 15m (c) 20m (d) 25m (e) 30m

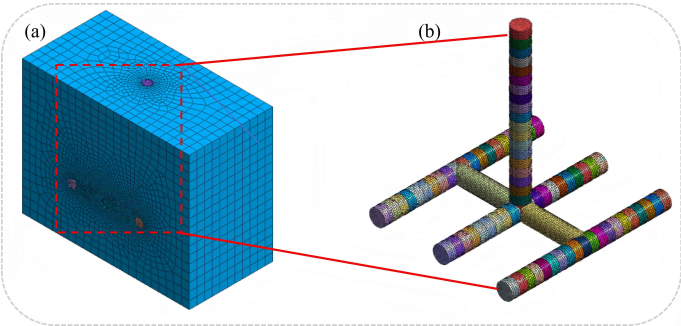


**Fig. 21** Numerical model of intersection area of circular tunnel (a) surrounding rock grid (b) intersection area grid

## 4 Discussion

In compressed air energy storage underground gas storage cavern complexes, intersection zones (e.g., shaft-chamber connections and tunnel junctions) constitute critical structural components where mechanical behaviors dominate, with their stability being paramount to the safe operation of the entire system. These regions typically serve as vulnerable areas for surrounding rock deformation and plastic zone development due to abrupt geometric transitions, stress concentrations, and cyclic loading effects.

A three-dimensional numerical model was established to investigate the stability of intersections involving shafts, connecting tunnels, and main chambers. The connecting tunnels comprised left and right branches. The numerical simulation considered main chambers at a burial depth of 200 m with chamber diameter of 5 m and inter-chamber spacing of 15 m. Stability analysis focused on shaft-tunnel-chamber intersections under maximum and minimum horizontal principal stress conditions. As illustrated in Fig.21, the model boundary conditions were defined by applying the maximum horizontal principal stress along the axis of the main chambers and the minimum horizontal principal stress perpendicular to the chamber walls. Through simulation of excavation sequences for underground chambers, connecting tunnels, and shafts under in-situ stress conditions, the stress field distribution and displacement patterns in surrounding rock masses were systematically analyzed.

Figs. 22-24 show the distribution characteristics of excavation stress and deformation responses at the intersection of the circular tunnel shaft, connecting roadways, and main chamber. It can be observed that for the left connecting roadway, the floor deformation is relatively significant, while for the right connecting roadway, the sidewall deformation is more pronounced. The overall deformation magnitude in the intersection zone remains at a relatively low level. Moreover, the stress concentration degree in this area is higher than that in the main chamber, with the maximum stress value reaching 8.83 MPa, which still does not reach the critical stress level required to induce stress-type failures. The distribution of plastic zones is crucial in evaluating the stability of underground cavern groups, optimizing support design, and guiding construction schemes. It is of great significance for ensuring engineering safety, optimizing design, and preventing disasters. From the plastic zone results, certain plastic deformations exist in the intersection area but remain within controllable limits. In terms of deformation magnitude, the stability of main chamber sidewalls shows no prominent influence from shaft intersection effects, specifically manifested by insignificant deformation level variations at intersection locations. Overall, the deformation magnitude in the intersection zone maintains a relatively low level.

Although the presence of shafts and connecting tunnels introduces certain perturbations to the stress distribution within the surrounding rock of the cavern group, the stress conditions required to induce stress-driven failure risks remain unmet. The primary potential instability mechanism persists as large deformations associated with the high sidewall configuration. Intersection effects exacerbate the free-surface conditions at adjacent rock masses, thereby reducing deformation stability. Given the cutting effects of structural plane development on rock integrity, the prerequisites for block failure formation are further amplified, necessitating enhanced reinforcement measures.

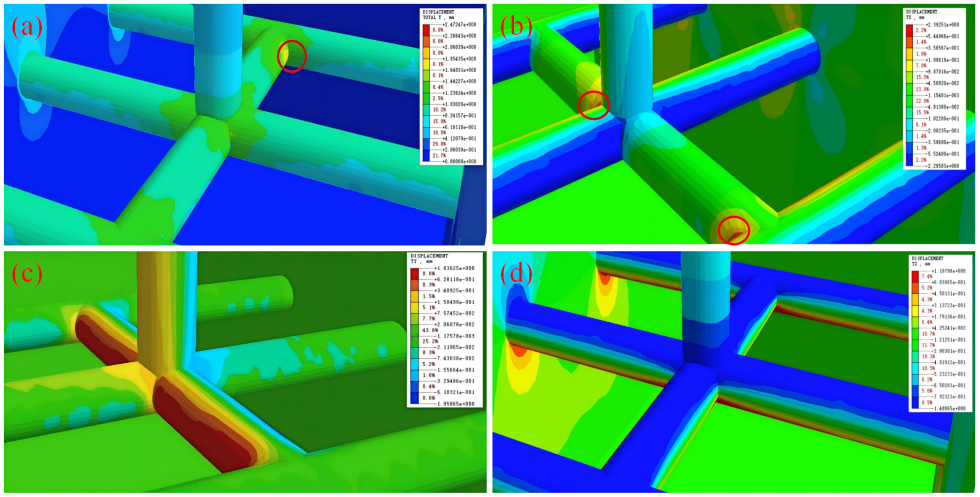


**Fig. 22** Displacement cloud of circular tunnel crossing area (a) Total displacement (b) X-direction displacement (c) Y-direction displacement (d) Z-direction displacement

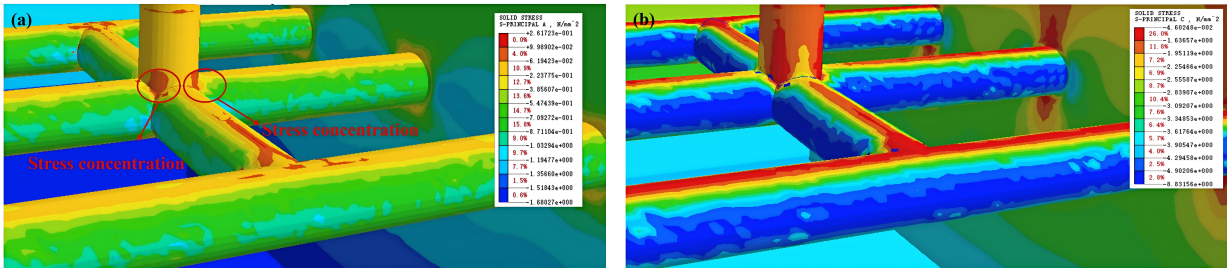


**Fig. 23** Stress clouds in the intersection area of circular tunnels (a) Maximum principal stresses (b) Minimum principal stresses

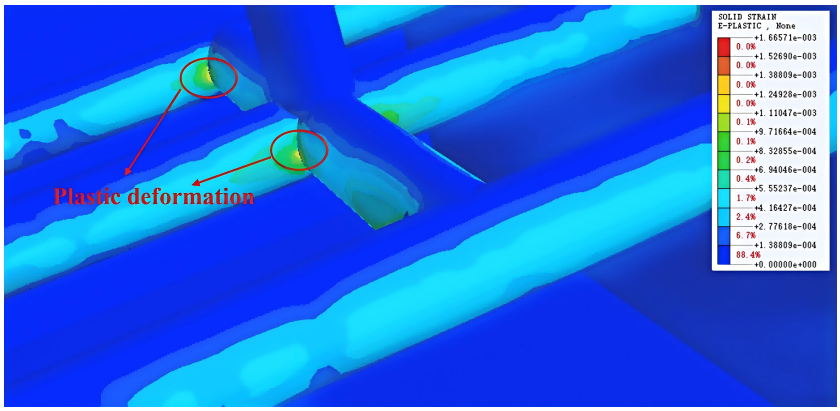


**Fig. 24** Plastic deformation cloud in the intersection area of circular tunnels

## 5 Conclusions

Through three-dimensional numerical simulations, this study systematically evaluates the impacts of burial depth, tunnel diameter, and spacing on deformation characteristics and plastic zone evolution in underground gas storage formations, with particular attention to intersection stability. Key findings are summarized as follows:

(1)Burial depth significantly affects the deformation and plastic zone distribution of gas storage surrounding rock. As burial depth increases, both vertical and horizontal displacements of surrounding rock decrease, with the rock mass transitioning gradually from plastic to elastic deformation. With increasing tunnel diameter, the horizontal displacement, vertical displacement, and vault vertical displacement of surrounding rock show continuous growth.

(2) Tunnel spacing exhibits relatively weaker influence on rock deformation and plastic zone distribution. As spacing increases, vertical and horizontal displacements of surrounding rock initially decrease before stabilizing.

(3) Considering economic efficiency and construction feasi-

bility under the assumed working conditions, the optimal layout parameters for gas storage clusters are determined as: 200 m burial depth, 5 m tunnel diameter, and 1.5D spacing when the storage pressure reaches 15 MPa.

(4) Although certain plastic deformations exist in intersection areas, all remain within controllable limits. Deformation monitoring reveals that the stability of main cavern sidewalls shows no significant impact from shaft intersections, as evidenced by negligible deformation variations at intersecting locations.

## Acknowledgements

This work was financially supported by the Key Projects of the fund of China petroleum pipeline engineering Co., Ltd. (No. 2023-20).

## Conflict of interest

The authors declare no competing interest.



## References

Budt M, Wolf D, Span R, et al. 2016. A review on compressed air energy storage: basic principles, past milestones and recent developments. *Applied Energy*, **170**: 250-268. doi:10.1016/j.apenergy.2016.02.108.

Chen LJ, Zheng TW, Mei SW, et al. 2016. Review and prospect of compressed air energy storage system. *Journal of Modern Power Systems and Clean Energy*, **4**(4): 529-541. doi:10.1007/s40565-016-0240-5.

Chen X, Wang JG. 2022. Stability analysis for compressed air energy storage cavern with initial excavation damage zone in an abandoned mining tunnel. *Journal of Energy Storage*, **45**, 103725. doi:10.1016/j.est.2021.103725.

Crotogino F, Mohmeyer KU, Scharf R. 2001. Huntorf CAES: more than 20 years of successful operation. *The Solution Mining Research Institute Spring Meeting*, Orlando, Orlando, 23-25 April 2001.

Fang J, Ma H, Yang C, et al. 2024. Airtightness evaluation of lined caverns for compressed air energy storage under thermo-hydro-mechanical (THM) coupling. *Energy*, **308**, 132996. doi:10.1016/j.energy.2024.132996.

Han Y, Cui H, Ma H, et al. 2022. Temperature and pressure variations in salt compressed air energy storage (CAES) caverns considering the air flow in the underground wellbore. *Journal of Energy Storage*, **52**: 104846. doi:10.1016/j.est.2022.104846.

Jia SP, Jin FM, Zheng DW, et al. 2015. Evaluation indices and classification criterion of aquifer site for gas storage. *Chinese Journal of Rock Mechanics and Engineering*, **34**(8): 1628-1640. doi:10.13722/j.cnki.jrme.2014.1197.

Li L, Liang WG, Lian HJ, et al. 2018. Compressed air energy storage: characteristics, basic principles, and geological considerations. *Advances in Geo-Energy Research*, **2**(2): 135-147. doi:10.26804/ager.2018.02.03.

Li Y, Li Y, Liu Y, et al. 2021. Compressed air energy storage in aquifers: basic principles, considerable factors, and improvement approaches. *Reviews in Chemical Engineering*, **37**: 561-584. doi:10.1515/revce-2019-0015.

Li P, Kang H, Zhu Q, et al. 2023. Numerical and experimental investigations of concrete lined compressed air energy storage system. *Journal of Cleaner Production*, **390**, 136153. doi:10.1016/j.jclepro.2023.136153.

Ma Y, Rao Q, Huang D, et al. 2022. A new theoretical model of local air-leakage seepage field for the compressed air energy storage lined cavern. *Journal of Energy Storage*, **49**, 104160. doi:10.1016/j.est.2022.104160.

Sun GH, Yi Q, Yao YF, et al. 2024. Study of potential instability modes in tunnel-type lined rock caverns of compressed air energy storage power plants. *Chinese Journal of Rock Mechanics and Engineering*, **43**(1): 41-49. doi:10.13722/j.cnki.jrme.2023.0199.

Sun GH, Wang J, Yu XY, et al. 2024. Research progress on basic principles and analysis methods of lined rock caverns for compressed air energy storage station. *Rock and Soil Mechanics*, **46**(1): 1-25. doi:10.16285/j.rsm.2024.0705.

Tooseh EK, Jafari A, Teymouri A. 2018. Gas-water-rock interactions and factors affecting gas storage capacity during natural gas storage in a low permeability aquifer. *Petroleum Exploration and Development*, **45**(6): 1123-1128. doi:10.1016/S1876-3804(18)30115-0.

Tunsakul J, Jongpradist P, Kongkitkul W, et al. 2013. Investigation of failure behavior of continuous rock mass around cavern under high internal pressure. *Tunnelling and Underground Space Technology*, **34**: 110-123. doi:10.1016/j.tust.2012.11.004.

Wang Z, Li W, Qiao L, et al. 2021. Effects of rate-dependent behavior of sandstone on performance of gas storage in aquifer. *Geomechanics for Energy and the Environment*, 100262. doi:10.1016/j.gete.2021.100262.

Xia CC, Zhou Y, Zhou SW, et al. 2015. A simplified and unified analytical solution for temperature and pressure variations in compressed air energy storage caverns. *Renew Energy*, **74**: 718-726. doi:10.1016/j.renene.2014.08.058.

Xu YJ, Zhou SW, Xia CC, et al. 2021. Three-dimensional thermo-mechanical analysis of abandoned mine drifts for underground compressed air energy storage: a comparative study of two construction and plugging schemes. *Journal of Energy Storage*, **39**, 102696. doi:10.1016/j.est.2021.102696.

Xu YJ, Xia CC, Zhou SW, et al. 2022. Anti-uplift failure criterion of caverns for compressed air energy storage based on the upper bound theorem of limit analysis. *Chinese Journal of Rock Mechanics and Engineering*, **41**(10): 1971-1980. doi:10.13722/j.cnki.jrme.2022.0018.

Yang CH, Wang TT, LI YY, et al. 2015. Feasibility analysis of using abandoned salt caverns for large-scale underground energy storage in China. *Applied Energy*, **137**:467-481. doi:10.1016/j.apenergy.2014.07.048.

Zhang XJ, Gao ZY, Zhou BQ, et al. 2024. Advanced Compressed Air Energy Storage Systems: Fundamentals and Applications. *Engineering*, **34**: 246-249. doi:10.1016/j.eng.2023.12.008.

Zhao K, Yang C, Ma H, et al. Daemen. 2023. A creep-fatigue model of rock salt and its application to the deformation analysis of CAES salt caverns. *Computers and Geotechnics*, **156**:105311. doi:10.1016/j.compgeo.2023.105311.

Zhao K, Ma H, Li H, et al. 2023. Stability analysis of CAES salt caverns using a creep-fatigue model in Yunying salt district, China. *Journal of Energy Storage*, **62**:106856. doi:10.1016/j.est.2023.106856.

Zhou SW, Xia CC, Du SG, et al. 2015. An analytical solution for mechanical responses induced by temperature and air pressure in a lined rock cavern for underground compressed air energy storage. *Rock Mechanics and Rock Engineering*, **48**(2): 749-770. doi:10.1007/s00603-014-0570-4.